Ocean Engineering 342 (2025) 123039

Contents lists available at ScienceDirect

Ocean Engineering

journal homepage: www.elsevier.com/locate/oceaneng

Research paper

Wave focusing and sheltering effects of a multi-layered cylindrical structure in regular wave conditions

Yuhao Cen [a], Dongfang Liang [a,*], Yifeng Yang [b], Xiaodong Liu [c]

[a] Department of Engineering, University of Cambridge, Cambridge, UK
[b] Department of Mechanical Engineering, University College London, London, UK
[c] College of Ocean Science and Engineering, Shandong University of Science and Technology, Qingdao, China

ARTICLE INFO

Keywords:
Wave focusing
Wave sheltering
Metamaterials
CFD
Shallow water flow
Wave energy

ABSTRACT

Inspired by the metamaterial superscatterer in electromagnetics, a multi-layered cylindrical structure has been proposed as an effective design for integrated breakwater–wave energy converter (WEC) systems, enabling both wave energy concentration and wave sheltering. In this study, a computational fluid dynamics (CFD) model is developed to investigate the wave dynamics around this structure, with the numerical predictions showing good agreement with the experimental measurements. A comparative analysis between the multi-layered and single-layered configurations is conducted, and the structure's performance is systematically evaluated with different water depths, wave frequencies, flume widths and wave heights. The results reveal the wave amplification factor of up to 3.6 due to refraction and superposition, while a downstream shadow zone emerges with an 80 % reduction of the wave height. Shallower or deeper water depths reduce the amplification and promote the early recovery of the incident wave profile, while wider flumes significantly extend the shadow zone due to the delayed reflection at the sidewalls. As the nonlinearity of the incident wave increases, both the amplification and sheltering effects are slightly weakened, and the shadow zone ends at a shorter distance from the structure, i.e., 3.2 times the cylinder diameter.

1. Introduction

Water waves are a type of mechanical wave, with gravity acting as the primary restoring force. Like electromagnetic (EM) waves, they are governed by the classical wave theory (Holthuijsen, 2010). Given that approximately 70 % of the Earth's surface is covered by oceans, water waves represent an abundant, clean, and renewable energy source. However, they can also pose significant threats to coastal and offshore structures due to impact forces, run-up and overtopping. This dual nature highlights the importance of developing effective water wave control strategies, with promising applications in wave energy harvesting (Scruggs and Jacob, 2009), coastal defence (Martinelli et al., 2008), and offshore structural protection (Lighthill, 1988).

Recent advances in artificially structured materials have shifted the focus of water wave research from passive defence to active control of wave propagation (Chen et al., 2009; Maurel et al., 2017). This direction draws inspiration from metamaterials originally developed in optics, electromagnetics, and acoustics (Cummer et al., 2016; Ma and Sheng, 2016; Sheng et al., 2003). Metamaterials are periodic structures composed of subwavelength artificial units, exhibiting unconventional properties such as negative refraction (Pendry, 2000; Smith et al., 2004), zero refractive index (Liberal and Engheta, 2017), reversed Doppler effect (Lee et al., 2010; Xiao and Qiu, 2005), and superlensing effect (Zhang and Liu, 2008). These properties have enabled the development of wave functional devices such as invisibility cloaks (Ma and Cui, 2010; Schurig et al., 2006; Shin et al., 2012), wave field rotators (Chen and Chan, 2007), illusion optics devices (Lai et al., 2009) and superscatterers (Qian et al., 2019).

Due to the formal similarity between the shallow water equations and Maxwell's equations, the concepts of metamaterials have been successfully extended to water wave control via effective parameter mapping (Cen et al., 2024a,b; Zhu et al., 2024). Through interaction with metamaterial-inspired structures, water waves can exhibit a variety of novel propagation behaviours, including wavefront rotation (Chen et al., 2009), wavelength modulation (Zhang et al., 2023), reflectionless guiding (Berraquero et al., 2013), and wave cloaking (Dupont et al.,

This article is part of a special issue entitled: Wave resonance phenomena published in Ocean Engineering.

* Corresponding author.
E-mail address: dl359@cam.ac.uk (D. Liang).

https://doi.org/10.1016/j.oceaneng.2025.123039
Received 3 August 2025; Received in revised form 21 September 2025; Accepted 29 September 2025
Available online 1 October 2025

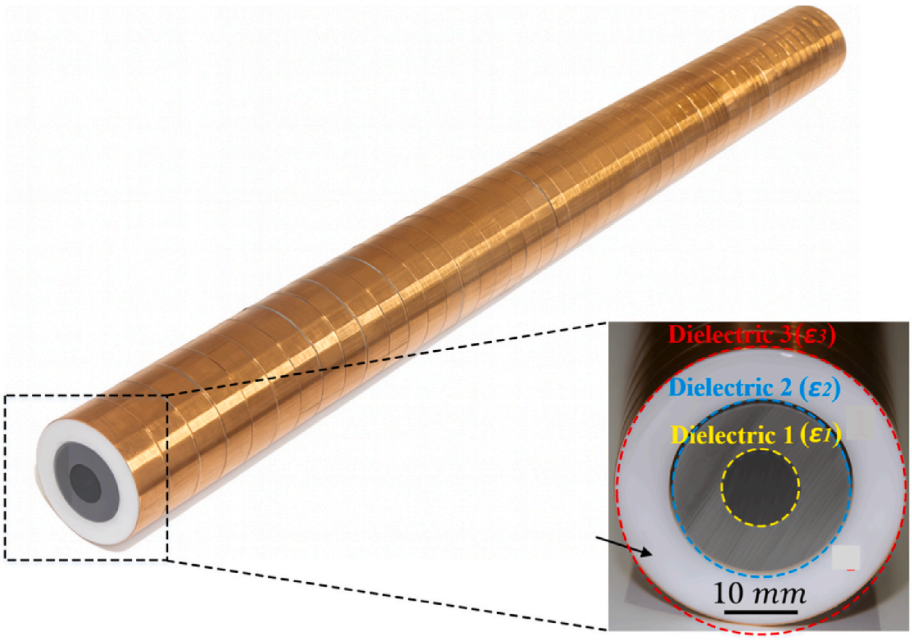

Fig. 1. Configuration of the electromagnetic superscatterer (Qian et al., 2019).

2015, 2016; Zareei and Alam, 2015).

Among these, wave focusing and sheltering have attracted particular interest due to their potential in developing hybrid breakwater–wave energy converter (WEC) systems. One early implementation of wave focusing employed a biconvex array of bottom-mounted cylinders, which acted as a lens to concentrate surface waves by adjusting the filling factor (Yang et al., 2009). To achieve direction-independent focusing, our previous work introduced an annular wave concentrator consisting of circularly arranged baffles with radially varying water depth (Cen et al., 2024a,b; Li et al., 2018). In parallel, a scattering-cancellation-based design was developed using concentric cylindrical rings, enabling energy concentration through constructive interference among diffracted waves (Zhang et al., 2020). For wave sheltering, shallow-water waveguides with gradient depth profiles have been proposed to redirect waves toward lateral platforms, creating a central region of minimal wave amplitude (Cen et al., 2024a,b; Zou et al., 2019). In addition to redistributing wave energy for sheltering purposes, mechanical metamaterial devices, such as periodic underwater oscillating resonators, have been used to dissipate wave energy by converting it into heat (De Vita et al., 2021). In addition to these approaches, wave focusing and sheltering phenomena have been jointly implemented in designs such as single- or twin-parabolic-arc pontoon breakwaters that rely on directed reflection; however, the location of the focal point is highly sensitive to wave frequency, which limits their practical application (Ren et al., 2021; Zhou et al., 2022). Most previous studies have addressed either wave focusing or wave sheltering effect in isolation, with the former concentrating on amplified waves and the latter on attenuated waves (Hao et al., 2022). A comprehensive assessment that integrates both the attenuated and amplified components remains scarce, limiting the practical advancement of breakwater–WEC hybrid systems (Calheiros-Cabral et al., 2025; Zhao et al., 2019). To address this gap, a multi-layered cylindrical structural design inspired by the metamaterial superscatterer for EM waves has recently been experimentally demonstrated to achieve both effects simultaneously (Qin et al., 2023). However, the study relied on two-dimensional (2D) EM analogue simulations, which neglected key hydrodynamic features such as three-dimensional flow effects, fluid viscosity, and nonlinearity. Moreover, it was limited to small-amplitude linear waves within a narrow flume, failing to capture the complexity of realistic ocean wave conditions.

In this study, we conduct three-dimensional computational fluid dynamics (CFD) simulations to explore the wave propagation characteristics around the multi-layered structure. To comprehensively evaluate its performance and identify the optimal operating condition, we perform a comparative analysis with a single-layered counterpart and systematically examine the effects of key factors—including wave frequency, water depth, flume width, and wave height—on both wave energy concentration and wave sheltering.

2. Structural design

2.1. Reference configuration for EM waves

The superscattering phenomenon was first experimentally demonstrated in a subwavelength, multi-layered rod (Qian et al., 2019). Superscattering refers to the pronounced enhancement of wave scattering enabled by engineered subwavelength structures, i.e., those with characteristic dimensions smaller than the wavelength of the incident waves. This allows physically small objects to capture or redistribute wave energy across a much broader spatial region, making it highly valuable for a range of practical applications, including antenna design, energy harvesting, biomedical imaging (e.g., magnetic resonance imaging, MRI), and wireless communications (Green and Pillai, 2012; Kinkhabwala et al., 2009; Loo et al., 2005; Waldman, 2001).

As shown in Fig. 1, this electromagnetic metamaterial consists of three concentric dielectric regions, referred to as Dielectric 1 (ε_1), Dielectric 2 (ε_2), and Dielectric 3 (ε_3), which are rolled into a cylindrical shape. Each region possesses a distinct electrical permittivity and, consequently, a different refractive index, enabling strong localisation and interaction of electromagnetic waves near the structure. The diameter of the rod remains much smaller than the incident wavelength, forming a subwavelength configuration suitable for enhanced scattering.

2.2. Analogy between electromagnetic and shallow-water wave systems

To extend the metamaterial concept to water wave control, a physical correspondence between the electromagnetic and shallow-water wave systems is established to guide the design of the water-wave counterpart. A Cartesian coordinate system (x, y, z) is adopted, where

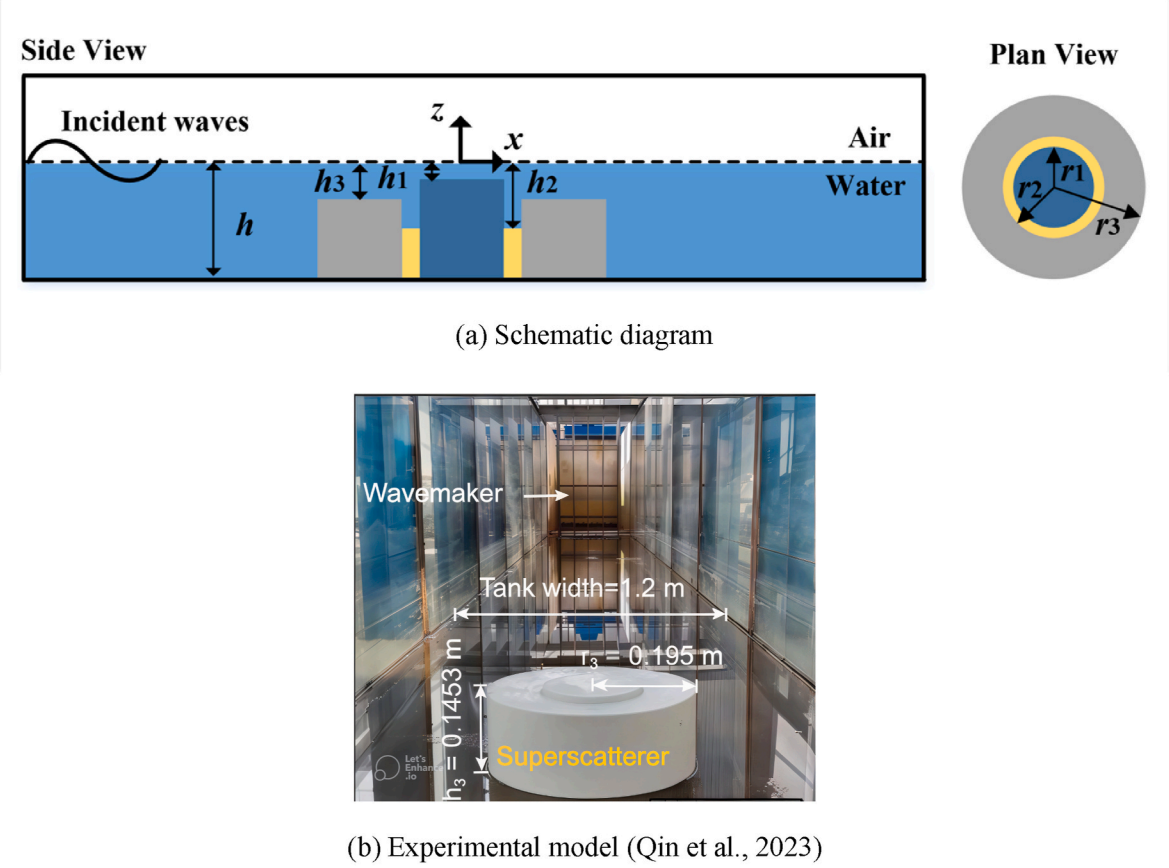

Fig. 2. Configuration of the multi-layered cylindrical structure.

x denotes the wave propagation direction, y is the transverse horizontal direction, and z is vertical, with the origin located at the mean water level.

In this section, the water is assumed to be inviscid and incompressible. The waves are considered to be of small amplitude, time-harmonic, and propagating under the shallow water condition, i.e., $kh \ll 1$, where k is the wavenumber and h is the mean water depth. Under these assumptions, the system is governed by the shallow water equations (Mei et al., 2005):

$$\frac{\partial \eta}{\partial t} + \nabla\cdot(hu_i) = 0, \tag{1}$$

$$\frac{\partial u_i}{\partial t} + g\nabla\eta = 0, \tag{2}$$

where t is time, $\eta = \eta(x,y)e^{i\omega t}$ is the free surface elevation, u_i are the fluid velocity components along the x (u_1), y (u_2), and z (u_3) directions, respectively, and g is the gravitational acceleration.

By combining Eqs. (1) and (2), the governing equation reduces to a Helmholtz-type form:

$$\nabla\cdot\left(\frac{h}{\rho}\nabla P\right) + \frac{\omega^2}{\rho g}P = 0, \tag{3}$$

where $P = \rho g\eta$ is the hydrostatic pressure at the free surface.

In comparison, the z-invariant Maxwell's equations for transverse magnetic (TM) EM waves are given by (Wang, 1986):

$$\nabla\cdot\left(\frac{1}{\varepsilon\varepsilon_0}\nabla H_z\right) + \mu\mu_0\omega^2 H_z = 0, \tag{4}$$

where $H_z = \frac{1}{\mu\mu_0}B_z$ is the z component of the magnetic field, B_z is the z component of the magnetic induction intensity, ε is the relative permittivity, ε_0 is the permittivity of vacuum, μ is the relative magnetic permeability, and μ_0 is the permeability of vacuum.

By comparing Eq. (3) and Eq. (4), an analogy can be drawn between the two systems, leading to the following correspondence of physical quantities:

$$H_z \leftrightarrow P, B_z \leftrightarrow \eta, \frac{1}{\varepsilon\varepsilon_0} \leftrightarrow \frac{h}{\rho}, \mu\mu_0 \leftrightarrow \frac{1}{\rho g}. \tag{5}$$

Based on this analogy, the spatial distribution of the permittivity shown in Fig. 1 can be physically realised in the water-wave context through a depth-modulated topography.

2.3. Depth-modulated counterpart for water waves

The water-wave counterpart to the EM configuration was recently demonstrated experimentally (Qin et al., 2023). In this implementation, a metamaterial-inspired structure was constructed using three concentric cylinders to produce spatially varying water depth. As illustrated in Fig. 2, the cylinders have radii of $r_1 = 0.0931$ m, $r_2 = 0.1000$ m, and $r_3 = 0.1950$ m, and heights of $h_1 = 0.1574$ m, $h_2 = 0.0701$ m, and $h_3 = 0.1453$ m, arranged from the innermost to outermost layer. This configuration creates four distinct fluid regions with depths of h-h_1, h-h_2, h-h_3 and h. The relative depth variation corresponds to the permittivity distribution in the reference configuration.

The system operates at a wave frequency of 1.55 Hz, corresponding to a wavelength of 0.60 m in water of depth 0.16 m. With an outermost diameter of only 0.65 times the wavelength, the structure satisfies the subwavelength condition and is expected to effectively reshape the uniform distribution of incident wave energy over a large area.

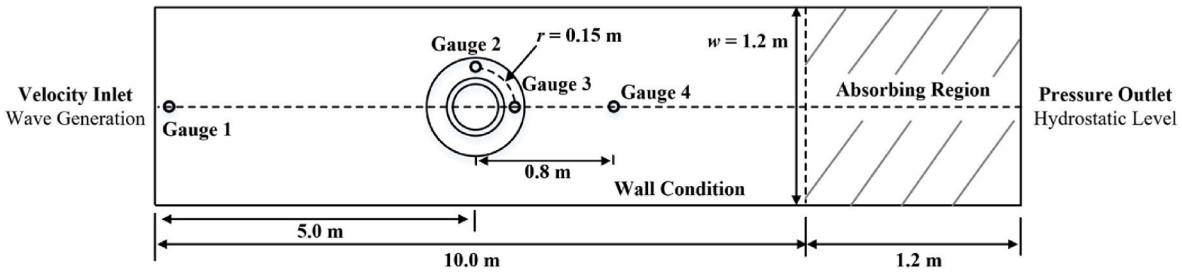

Fig. 3. Domain setup of the NWT with the structure.

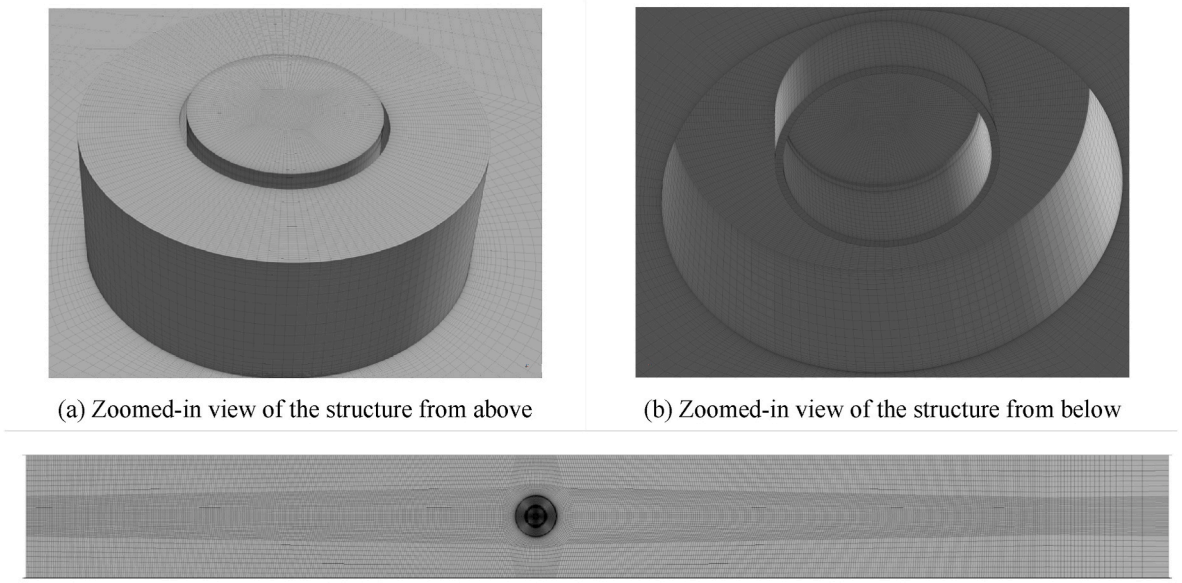

Fig. 4. Mesh for the CFD simulations.

3. Numerical model and validation

3.1. Governing equations

The numerical simulations of the incompressible viscous shallow water flows are conducted by solving the Navier-Stokes equations (Constantin and Foiaş, 1988):

$$\frac{\partial u_i}{\partial x_i} = 0, \tag{9}$$

$$\frac{\partial u_i}{\partial t} + u_j\frac{\partial u_i}{\partial x_j} = -\frac{1}{\rho}\frac{\partial p}{\partial x_i} + \frac{\partial}{\partial x_j}\left[\nu\left(\frac{\partial u_i}{\partial x_j} + \frac{\partial u_j}{\partial x_i}\right)\right] + g_i, \tag{10}$$

where t is time, ν is the kinematic viscosity coefficient of the fluid, ρ is the fluid density, and p is the pressure.

In addition, the Volume of Fluid (VOF) multiphase flow model is employed, as it is well-suited for simulating flows involving two or more immiscible fluids. This model is particularly effective in capturing surface gravity wave propagation at the air–water interface. By tracking the volume fraction of each phase, it accurately identifies the location of the interface between the fluids. The volume fraction of phase i is defined as:

$$\alpha_i = \frac{V_i}{V}, \tag{9}$$

where V_i is the volume of phase i in the computational cell, and V is the total cell volume. Within a computational cell, the sum of the volume fractions of all phases must equal 1, as given by:

$$\sum_{i=1}^{N} \alpha_i = 1, \tag{9}$$

where N is the total number of phases, which is 2 in this study. Based on the computed volume fractions, the phase distribution within each cell can be determined as follows:

$$\begin{cases} 0 < \alpha_i < 1 : \text{water–air interface} \\ \alpha_i = 0 : \text{air} \\ \alpha_i = 1 : \text{water} \end{cases}. \tag{9}$$

3.2. Computational domain and boundary conditions

Fig. 3 illustrates the numerical wave tank (NWT), which contains the cylindrical structure under investigation. The tank measures 11.2 m in length, 1.2 m in width, and 0.2 m in height. Within the computational domain, the testing region spans 10 m. Downstream of this region, a 1.2 m-long wave-absorbing zone is included—approximately twice the operating wavelength—to minimise wave reflection from the outlet boundary. To implement this, a source term is introduced into Eq. (10) near the outlet boundary (Fluent, 2011), defined as:

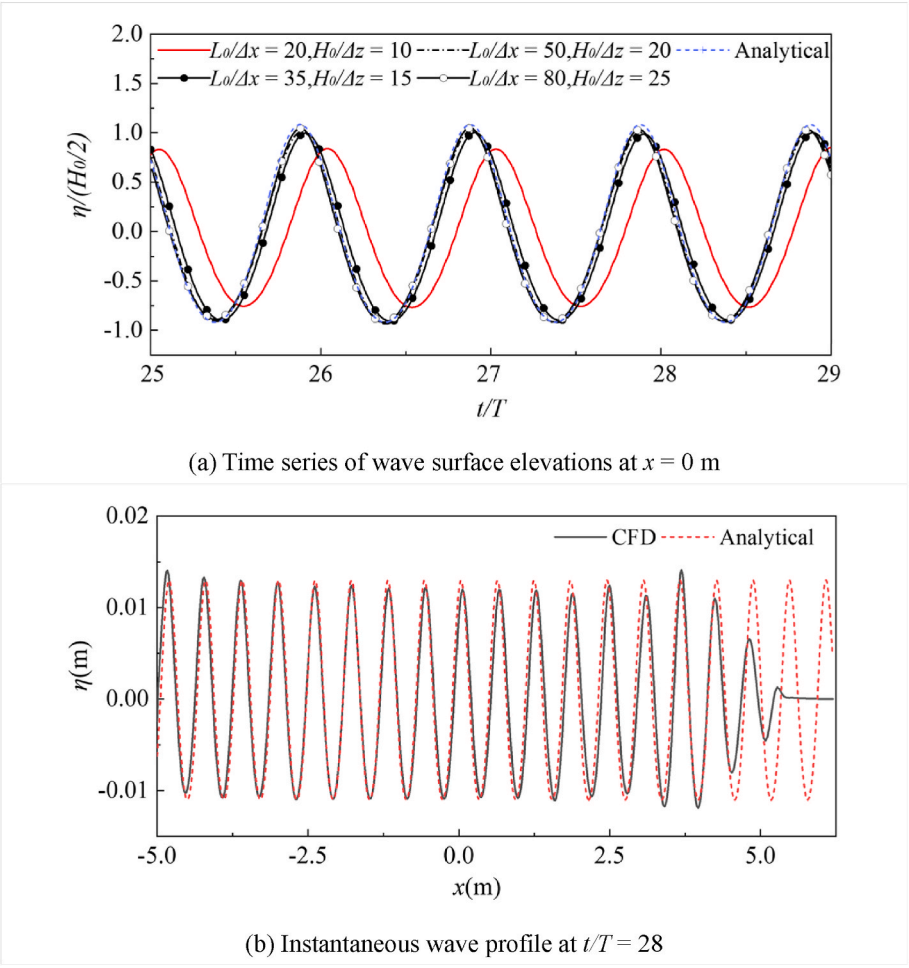

Fig. 5. Mesh independence test without the structure.

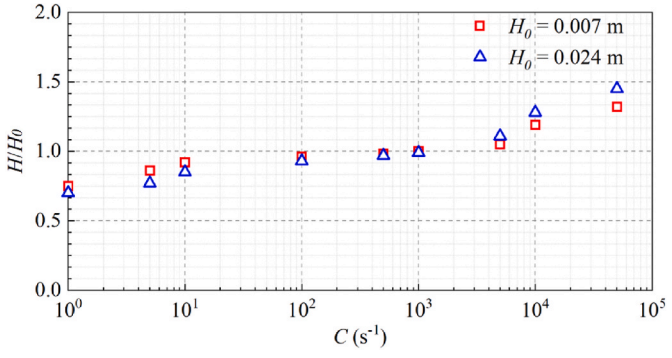

Fig. 6. Averaged wave heights for different damping coefficient values.

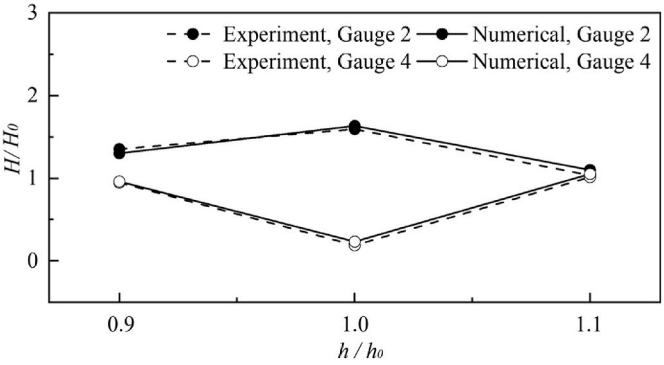

Fig. 7. Comparison between experimental and numerical results.

$$S = \begin{cases} 0 \quad for\ x \le x_1\ or\ x \ge x_2 \\ -C\rho u_3\left(1-\dfrac{z-z_1}{z_2-z_1}\right)\left(\dfrac{x-x_1}{x_2-x_1}\right)^2 for\ x_1 < x < x_2 \end{cases}, \tag{12}$$

where u_3 is the vertical water velocity, x_1, x_2 denote the start and end positions of the absorbing region in the streamwise direction, z_1, z_2 are the free surface and bed elevations, respectively, and C is an empirical coefficient.

Waves are generated by prescribing a velocity-inlet condition at the inflow boundary. At each time step, the free surface elevation and corresponding flow velocity are computed according to the appropriate wave theory, selected based on the wave steepness and relative wave height. A no-slip wall condition is applied to the sidewalls, bottom of the wave tank, and the surface of the structure. At the top of the domain, a pressure-outlet boundary condition is imposed with pressure fixed at the atmospheric level. At the outlet, a pressure-outlet boundary condition is also used, where the pressure is defined based on the local free-surface level extrapolated from the volume fraction values of the neighbouring cells.

To monitor the free surface elevation variations within the testing region, wave gauges are positioned along or adjacent to the flume centreline. Gauge 1 is located near the inlet to verify that the generated

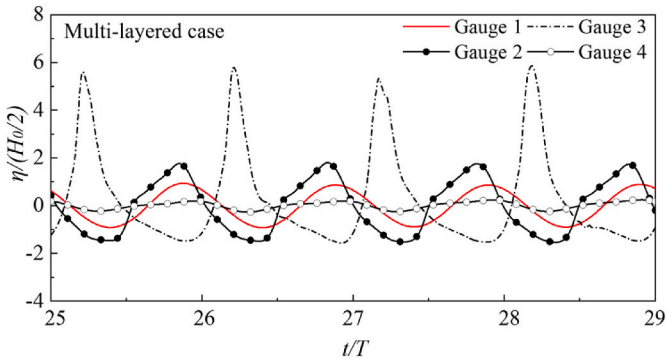

Fig. 8. Free surface elevations around the multi-layered structure.

wave profile aligns with the chosen wave theory. Gauges 2 and 3 are placed beside and downstream of, respectively, the innermost cylinder at a radial distance of 0.15 m from its centre to capture local wave amplification induced by the structure. Gauge 4 is situated 0.8 m downstream of the cylinder centre to assess the wave sheltering effect.

3.3. Numerical implementation

A structured hexahedral mesh is generated throughout the computational domain using the commercial software ANSYS ICEM CFD, as shown in Fig. 4. To accurately track the free water surface, the mesh is gradually refined in the vertical direction from the top and bottom boundaries towards the still water level. Finer cells are also concentrated around the structure to better resolve the complex local wave fields.

The simulations are carried out using the commercial CFD software ANSYS Fluent. A transient pressure-based solver is adopted, incorporating the Pressure Implicit with Splitting of Operators (PISO) algorithm, which efficiently handles pressure–velocity coupling in unsteady free-surface flows. No turbulence models are applied due to the low wave amplitude considered in the study. Suitable spatial discretisation schemes are applied to the gradient, pressure, momentum, and volume fraction fields. Gradient approximation uses the Least Squares Cell-Based method, which reduces discretisation errors through a least-squares approach. Momentum discretisation employs the third-order Monotone Upstream-Centred Scheme for Conservation Laws (MUSCL), providing high spatial resolution for complex three-dimensional flows. Pressure interpolation uses the PREssure STaggering Option (PRESTO!) scheme in ANSYS Fluent (2011), which is designed to resolve sharp pressure gradients accurately. The Geo-Reconstruct scheme is used to capture phase interfaces in multiphase flow regions.

All simulations are performed on a high-performance computing platform equipped with 56 Intel Xeon E5-2680 v4 CPU cores and 128 GB of memory. Each case comprises approximately five million mesh cells and typically requires around 45 h to complete using parallel processing in ANSYS Fluent. Following an initial transient phase of 25 wave cycles, output from four representative wave periods ($t = 25T$–$29T$) is selected for post-processing and analysis.

3.4. Mesh independence study

To determine the optimal mesh cell size, a mesh independence study is conducted using the numerical wave tank without the presence of the cylindrical structure. The study evaluates how different mesh resolutions affect the simulated free surface elevations under the consistent incident wave condition, defined by a wave period $T = 0.645$ s, wave height $H_0 = 0.024$ m, water depth $h = 0.16$ m, and wavelength $L_0 = 0.6$ m. This case represents the most demanding scenario considered in the present study, as it corresponds to the highest wave height examined.

In the streamwise direction, the mesh cells are uniformly distributed with a size of Δx in the testing region, gradually coarsening in the wave-absorbing section. In the vertical direction, a constant cell size of Δz is applied within a zone extending one wave height above and below the still water level, beyond which the mesh resolution decreases progressively. Four mesh resolutions are tested, with $L_0/\Delta x$ and $H_0/\Delta z$ ranging from 20 to 80 and 10 to 25, respectively. In addition, following an assessment of time step sensitivity, a time step of $T/1000$ is selected to ensure accuracy and stability.

Fig. 5 presents the time series of free surface elevations at different mesh resolutions. The water levels are normalised by half of the incident wave height, $H_0/2$. It is observed that, except for the coarsest mesh case ($L_0/\Delta x = 20$, $H_0/\Delta z = 10$), which exhibits significant numerical

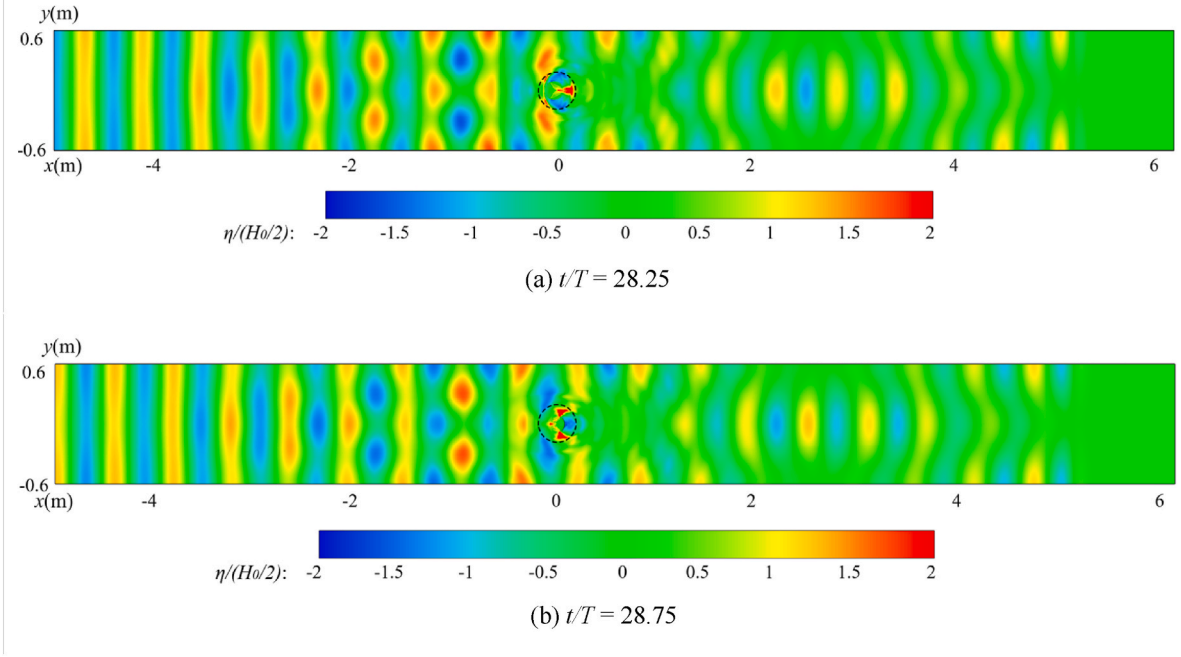

Fig. 9. Free surface elevation distributions over the computational domain.

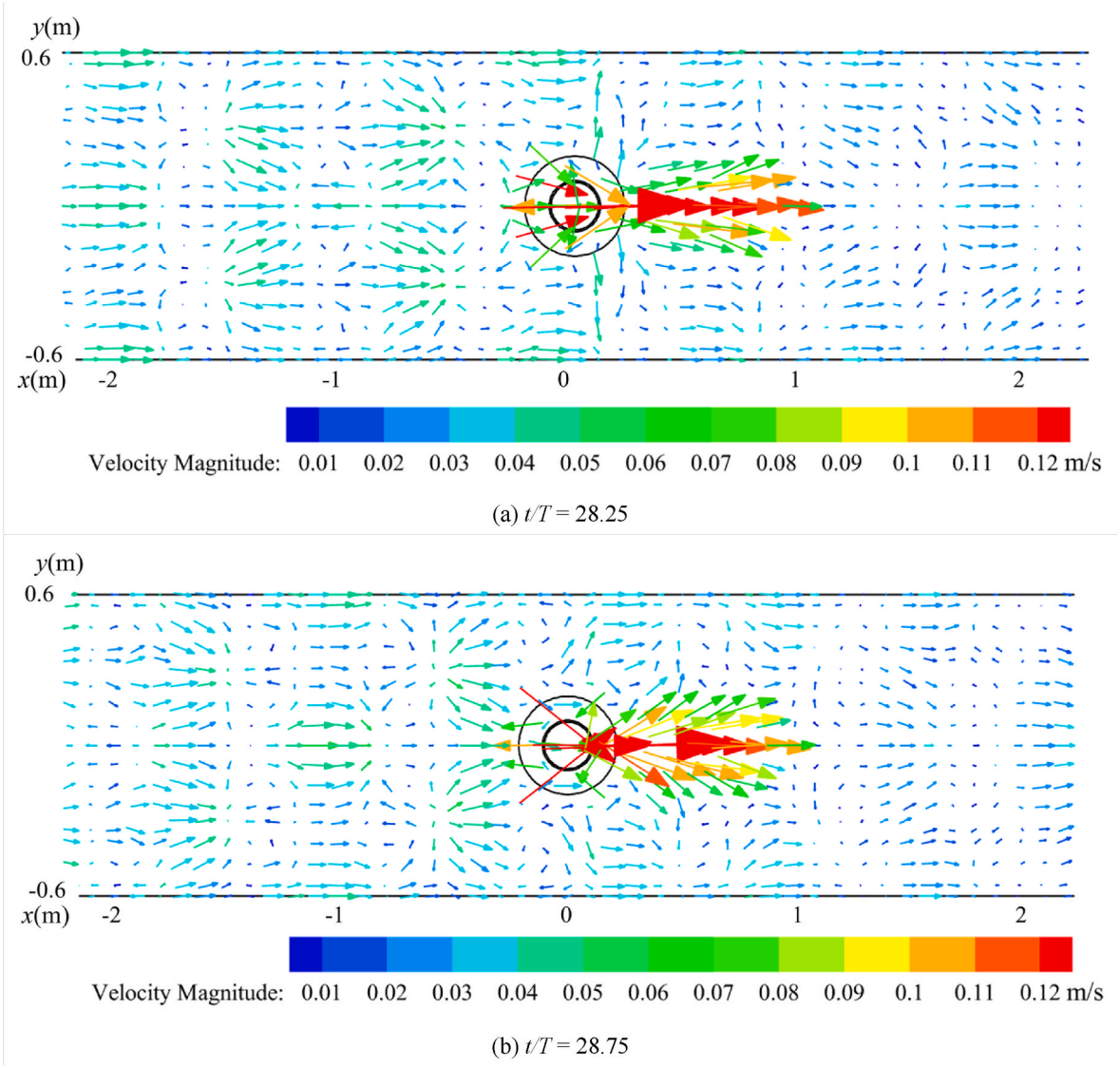

Fig. 10. Velocity fields at the still water level around the multi-layered structure.

damping, the other three cases closely match the analytical solution. For the coarsest mesh, the averaged deviation in wave height reaches approximately 21 %. In contrast, the finer meshes maintain deviations within 5 %, indicating improved accuracy with a finer resolution. To achieve a good balance between accuracy and computational cost, a resolution of $L_0/\Delta x = 35$ and $H_0/\Delta z = 15$ is adopted for subsequent simulations. Fig. 5(b) shows the instantaneous wave profile at $t/T = 28$ for the selected resolution, demonstrating effective wave absorption near the outlet boundary.

The damping intensity of the wave-absorbing zone depends on the coefficient C in Eq. (12). Therefore, a sensitivity analysis of C is performed in the numerical wave tank without the presence of the structure to determine its optimal value for effective wave absorption. We consider two design wave scenarios: a Stokes wave with height $H_0 = 0.024$ m and a linear wave with $H_0 = 0.007$ m, both with the frequency ($f = 1.55$ Hz) and water depth ($h = 0.16$ m). Fig. 6 shows the averaged wave heights (normalised by H_0) at gauge 4 for different coefficient values. When C is too small (1, 5, 10 s^{-1}), insufficient wave absorption allows residual waves from the outlet boundary to re-enter the domain and interfere with the incident waves, leading to a predicted wave height smaller than the prescribed incident wave. Conversely, when C is too large ($C = 5000$, 10000, 50000 s^{-1}), strong reflections occur at the entrance of the numerical beach, which results in an overestimated wave height. Based on these results, $C = 1000$ s^{-1} is chosen to ensure that waves are smoothly absorbed without disturbing the propagation in the domain.

3.5. Model validation

The cylindrical structure was fabricated via 3D printing, as detailed in a previous study (Qin et al., 2023). The experimental wave tank measured 60 m in length, 1.2 m in width, and 2 m in depth. The structure was firmly secured to the bottom of the tank using adhesive. A wave maker was installed at the upstream end, while a wave-absorbing material was placed at the downstream end. The tank had rigid glass walls along both sides to ensure lateral confinement.

To investigate the influence of water depth on the wave structure interaction, the water depth was varied between 0.15 m and 0.17 m during the experiments. The linear wave condition was ensured by maintaining the wave height below 1/50 of the wavelength. It was verified that the target wave heights could be accurately generated and measured using wave probes with a fine resolution of 0.1 mm in the same experimental facility (Li et al., 2018; Qin et al., 2023; Zou et al., 2019). All parameters were carefully controlled to maintain wave

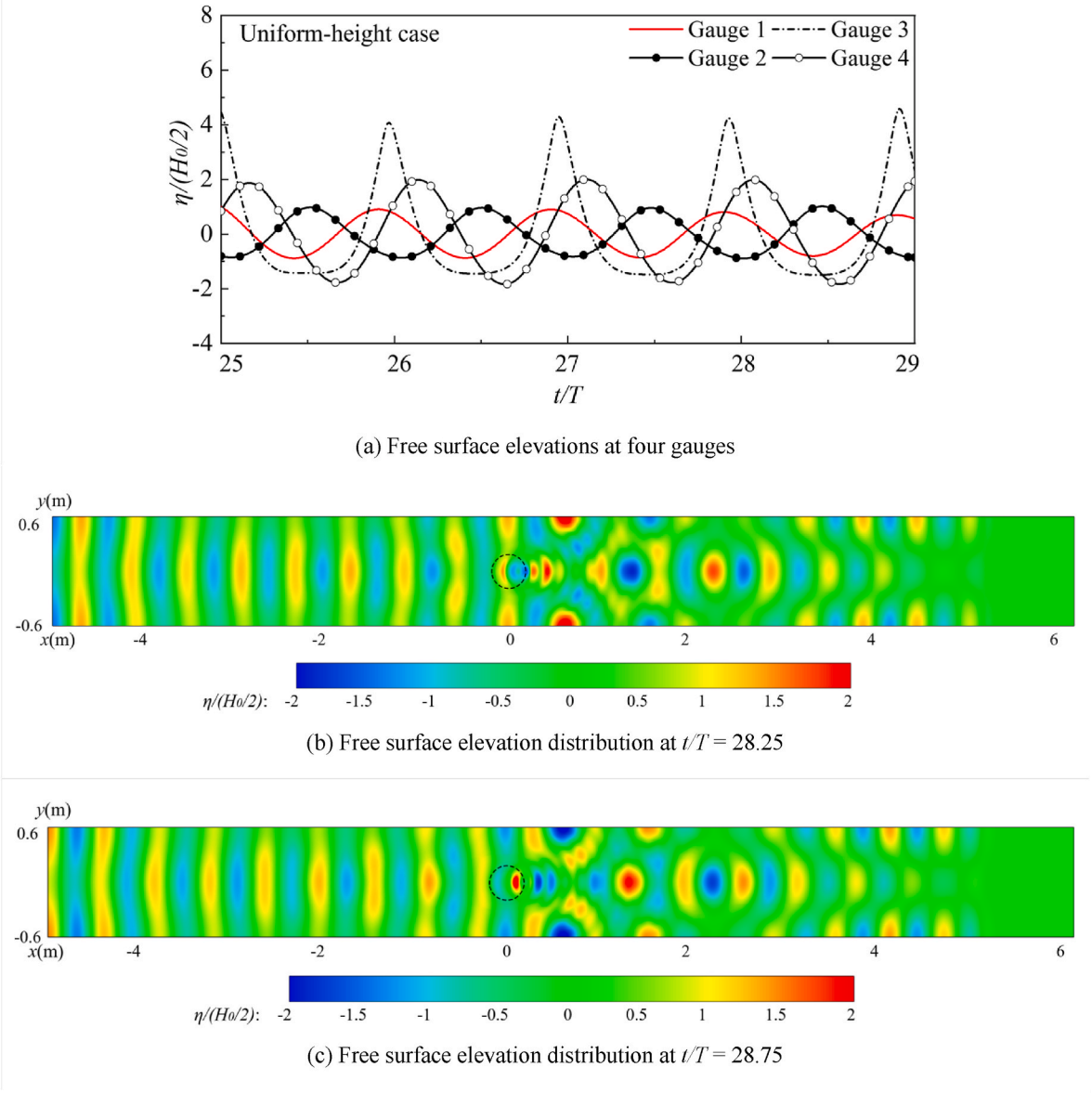

Fig. 11. Details of the wave field around the single-layered configuration.

linearity, and measurements were conducted only after the wave field had stabilised, thereby minimising transient and nonlinear effects. Laminar flow was consistently observed, and the water surface remained free of irregular disturbances throughout the experiments. The use of a small boat further confirmed the desired wave property, as its vertical motion was sinusoidal and closely matched the amplitude of the incoming waves. The structure was placed 15 m downstream from the wave maker and 45 m upstream of the wave absorber, ensuring that the influence of reflected waves was minimised. Wave amplitudes were recorded at two positions corresponding to the numerical gauge locations (gauges 2 and 4).

The numerically predicted wave heights at gauges 2 and 4 are compared with the experimental data in Fig. 7, where wave heights are normalised by the incident wave height $H_0 = 0.007$ m and water depths are normalised by the designed water depth $h_0 = 0.16$ m. The results show good agreement across all water depths, demonstrating the model's ability to accurately reproduce the transformed wave fields around the cylindrical structure. The root-mean-squared errors (RMSE) between the numerical and experimental results are calculated. At gauge 2, the RMSE is approximately 0.053, while at gauge 4, it is 0.035, indicating satisfactory accuracy at both locations.

4. Results and discussion

4.1. Performance comparison of multi-layered and single-layered configurations

Simulations of the wave fields around the multi-layered cylindrical structure are performed. Linear waves with a height of $H_0 = 0.007$ m, a water depth of $h = 0.16$ m, a frequency of $f = 1.55$ Hz, and a wavelength of $L_0 = 0.60$ m are fed to the computational domain. After an initial transient phase of 25 wave cycles, the system reaches a steady state, and the free surface elevations are recorded at multiple gauge positions. In this section, all water levels are normalised by half of the incident wave height, $H_0/2$.

The recorded wave profiles differ substantially across the four gauges, reflecting the distinct evolution of the wave field around the structure. Near the inlet (gauge 1), the wave profile closely follows the linear wave theory, confirming negligible influence from wave reflection due to the downstream structure. Significant wave amplification is

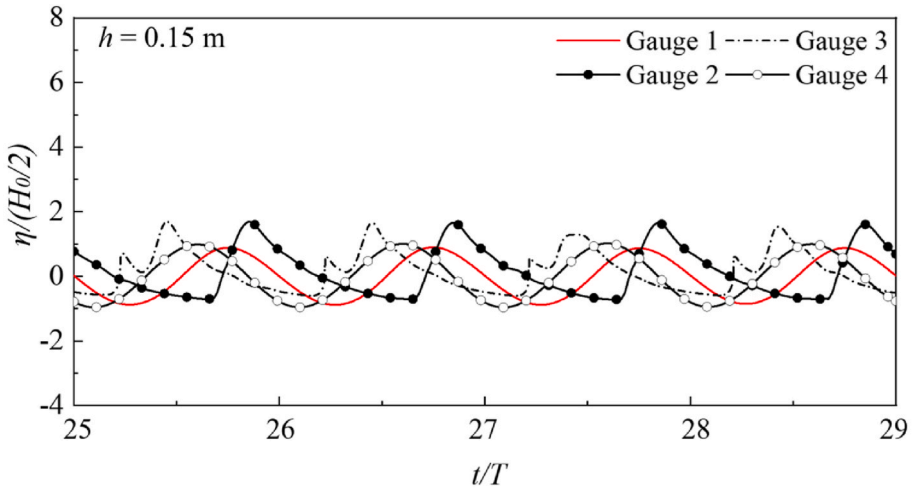

(a) $h = 0.15$ m

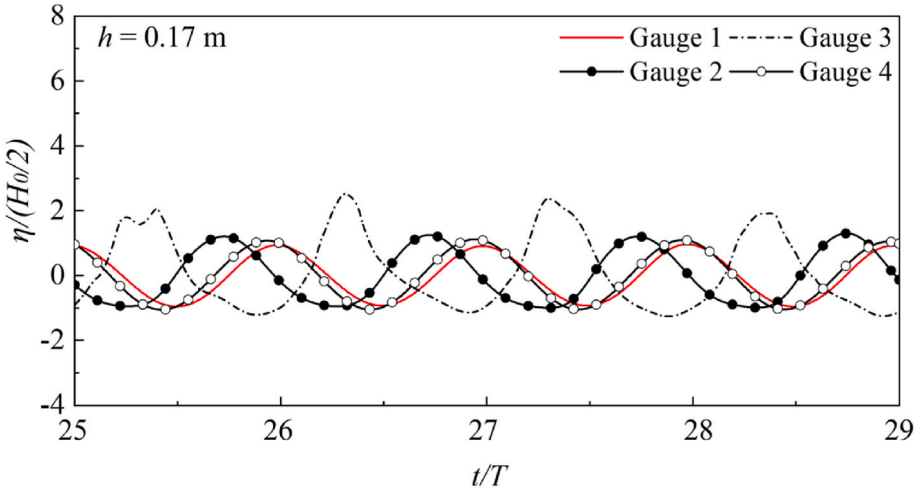

(b) $h = 0.17$ m

Fig. 12. Free surface elevations at different water depths.

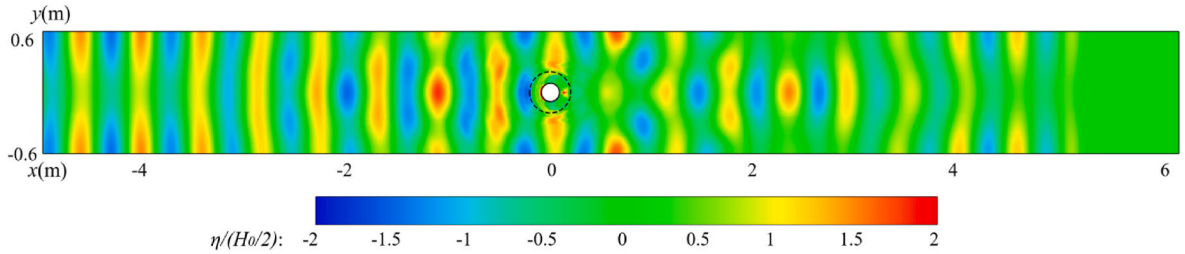

Fig. 13. Free surface elevation distribution for $h = 0.15$ m at $t/T = 28.25$.

observed over the cylinder. At gauge 2 (beside the innermost cylinder) and gauge 3 (behind the cylinder), the wave heights reach 1.6 and 3.6 times the incident wave height, respectively. This indicates that a stronger wave energy concentration occurs behind the cylinder, which is a location not originally monitored in the experimental setup. Meanwhile, the waveform at gauge 3 exhibits pronounced nonlinear features, with a mean disparity between the crest and trough heights reaching 73 %, characterised by sharp crests and flat troughs. Beyond the structure, at gauge 4, the wave height is reduced by approximately 80 % compared to the incident wave height, highlighting the structure's effectiveness in redistributing wave energy.

The free surface elevation distributions at different instants within a wave cycle are presented in Fig. 9. The interaction between the incident wave and the cylinder generates short-crested wave patterns around the structure. Upstream of the structure, these features primarily result from local wave reflection. As the wave reaches the outermost cylinder, outlined by dashed circles, wavefront bending becomes immediately apparent due to depth-induced refraction. This leads to spatial variations in phase velocity, focusing wave energy within the structure. This effect is particularly prominent along the sides of the innermost cylinder

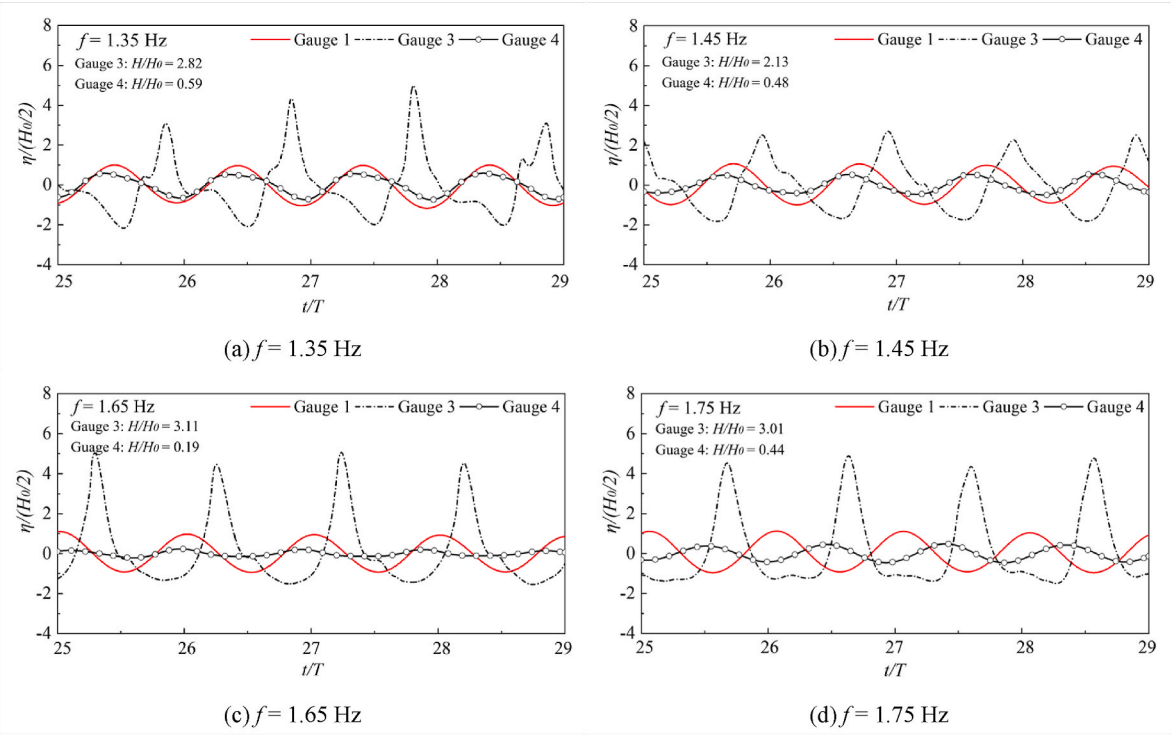

Fig. 14. Free surface elevations at different wave frequencies.

and behind it, consistent with the wave amplification observed at gauges 2 and 3.

Downstream of the structure, a wave shadow zone emerges, characterised by a pronounced reduction in wave amplitude, followed by a gradual recovery toward the incident wave amplitude. This zone extends approximately 2 m in streamwise length, corresponding to about five times the diameter of the outermost cylinder. This sheltering effect likely results from the nonlinear interactions among the refracted wave components.

To gain further insight into the nonlinear wave interactions, Fig. 10 presents the velocity fields adjacent to the structure at the same instants. Given that the vertical momentum and its variation remain small under the present shallow-water condition, and that the wave pattern transformation around the structure is primarily governed by the horizontal refraction and reflection, the velocity fields are extracted along a horizontal slice at the still water level. This representation is considered sufficient since horizontal velocity components dominate the flow and effectively capture the key features of momentum redistribution induced by the structure. As the wave propagates over the structure, refraction redirects fluid particles toward the flume centreline. Consequently, their oscillatory motion intensifies significantly, with the flow velocity peaking near the rear end of the outermost cylinder.

In the wave shadow zone, despite the substantial reduction in wave amplitude, a local increase in fluid particle velocity is observed. This phenomenon indicates that the decrease in wave height—and thus potential energy—is accompanied by a corresponding increase in kinetic energy, intensifying the downstream fluid motion. This effect is likely driven by the destructive interference among the refracted wave components, which modulates the local velocity field. As the wave propagates further, this effect is weakened, and the flow velocity gradually returns to its unperturbed pattern.

In comparison, Fig. 11 displays a distinct wave pattern around the single-layered configuration, characterised by a constant cylinder diameter r_3 and height h_3. The same mesh resolution and incident wave condition are applied to ensure a consistent basis for comparison with the multi-layered configuration. As shown in Fig. 11(a), wave amplification is less pronounced, with the wave height remaining equal to the incident height at gauge 2 and increasing to only 2.7 times the incident height at gauge 3. Unlike the multi-layered case, where wave height attenuation occurs downstream, the wave amplitude at gauge 4 increases to 1.8 times the incident amplitude.

Fig. 11(b) and (c) illustrate the evolution of the wave field, offering insight into the mechanism behind the differing wave pattern. Wave energy is concentrated near the rear end of the cylinder, and significant reflection at the sidewalls is observed after the wave passes the structure. These reflected waves undergo constructive interference, leading to an increase in wave amplitude. This highlights a key distinction from the multi-layered configuration, where a pronounced shadow zone develops downstream.

4.2. *Effect of water depth*

The impact of water depths of 0.15 m and 0.17 m on the wave dynamics around the structure is examined, with the corresponding free surface elevations at various gauges shown in Fig. 12. In both cases, wave amplification over the structure (at gauges 2 and 3) is much less pronounced, suggesting a reduced wave focusing effect. Notably, at gauge 3, the wave heights reach approximately 1.1 and 1.7 times the incident wave height for the shallower and deeper water cases, respectively. Downstream, the wave profiles at gauge 4 closely match the incident wave pattern, indicating an earlier recovery of the downstream wave to the incident profile at both depths.

In addition, compared with the fully submerged configurations where the wave amplitude increases as the wave travels from the cylinder's side to its rear, the case of $h = 0.15$ m shows no significant difference in amplitude between gauges 2 and 3. Both locations display enhanced waveform asymmetry, indicating a diffraction-dominated pattern under this shallow water condition.

These phenomena result from the depth–induced changes in reflection, refraction, and diffraction. At $h = 0.15$ m, the surface-piercing cylinder enhances wave reflection, modifies refraction angles due to a more abrupt depth transition, and strengthens diffraction, causing a

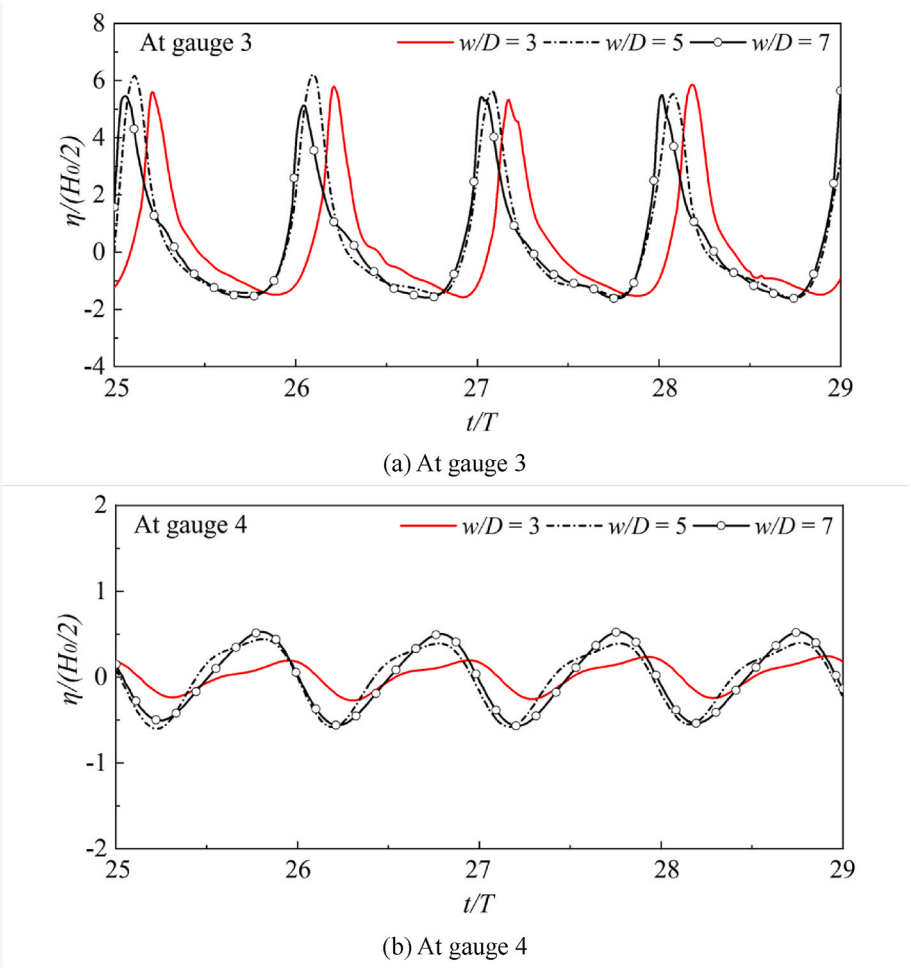

Fig. 15. Free surface elevations at different flume widths.

greater portion of wave energy to spread laterally rather than concentrate within the structure. In contrast, at $h = 0.17$ m, the less pronounced depth variation weakens both reflection and refraction effects, allowing the waves to propagate more directly with largely unaltered straight wavefronts.

As shown in Fig. 13, the enhanced diffraction at the shallower depth leads to a different free surface elevation distribution compared to the case of $h = 0.16$ m. Wavefront bending is confined to a local region above the cylinder, while diffraction dominates the wave propagation. The transmitted waves travel smoothly along both sides of the structure, maintaining a consistent phase. Further downstream, the wave pattern rapidly returns to its incident form, resulting in a reduction in the shadow zone length by a half of that with the designed water depth. These results indicate that the structure's wave focusing and sheltering performance are highly sensitive to the water depth.

4.3. Effect of wave frequency

The sensitivity of the structure's performance to wave frequency is assessed for $f = 1.35$, 1.45, 1.65 and 1.75 Hz. As shown in Fig. 14, the amplification and reduction factors (H/H_0) for gauges 3 and 4 are annotated in each sub-plot for clarity. The structure performs effectively over a moderate frequency bandwidth, with the wave amplitude enhanced to approximately 2–3 times the incident amplitude above the cylinder and generally suppressed to below 60 % of the incident amplitude in the shadow zone. The higher frequency cases exhibit greater amplification at gauge 3, accompanied by increased waveform asymmetry, and stronger attenuation at gauge 4 compared to the lower frequency ones. Among all cases, the configuration performs best at $f = 1.55$ Hz, achieving the most effective combination of wave focusing and downstream sheltering, with an amplification factor of 3.60 at gauge 3 and a reduction factor of 0.21 at gauge 4, as shown in Fig. 8.

4.4. Effect of flume width

As shown in Fig. 9, when the wave leaves the structure, part of the wave is redirected laterally toward the sidewalls, where subsequent reflection contribute to the downstream energy redistribution. To investigate the influence of the lateral wave reflection, we increase the flume width w from 1.2 m to 2.0 m and 2.8 m, corresponding to the width-to-diameter ratio $w/D = 3$, 5 and 7, respectively, where $D = 0.39$ m is the diameter of the outermost cylinder.

Fig. 15 presents the free surface elevations at gauges 3 and 4 for different flume widths. All cases with varying w/D exhibit similar levels of wave amplification over the structure and attenuation in the wave shadow zone. While the wave amplitude at gauge 4 slightly increases as the flume widens, it remains at approximately 50 % of the incident amplitude. These results indicate that variations in flume width have a limited influence on the free surface elevations at the measured locations.

However, the free surface elevation distributions for the wider flume cases, shown in Fig. 16, reveal notable differences in the downstream wave patterns. As the flume width increases, the wave shadow zone extends significantly farther. This extension occurs because the waves can travel longer distances before interacting with the sidewalls, thereby delaying the onset of lateral reflection. In the case of $w/D = 5$, the

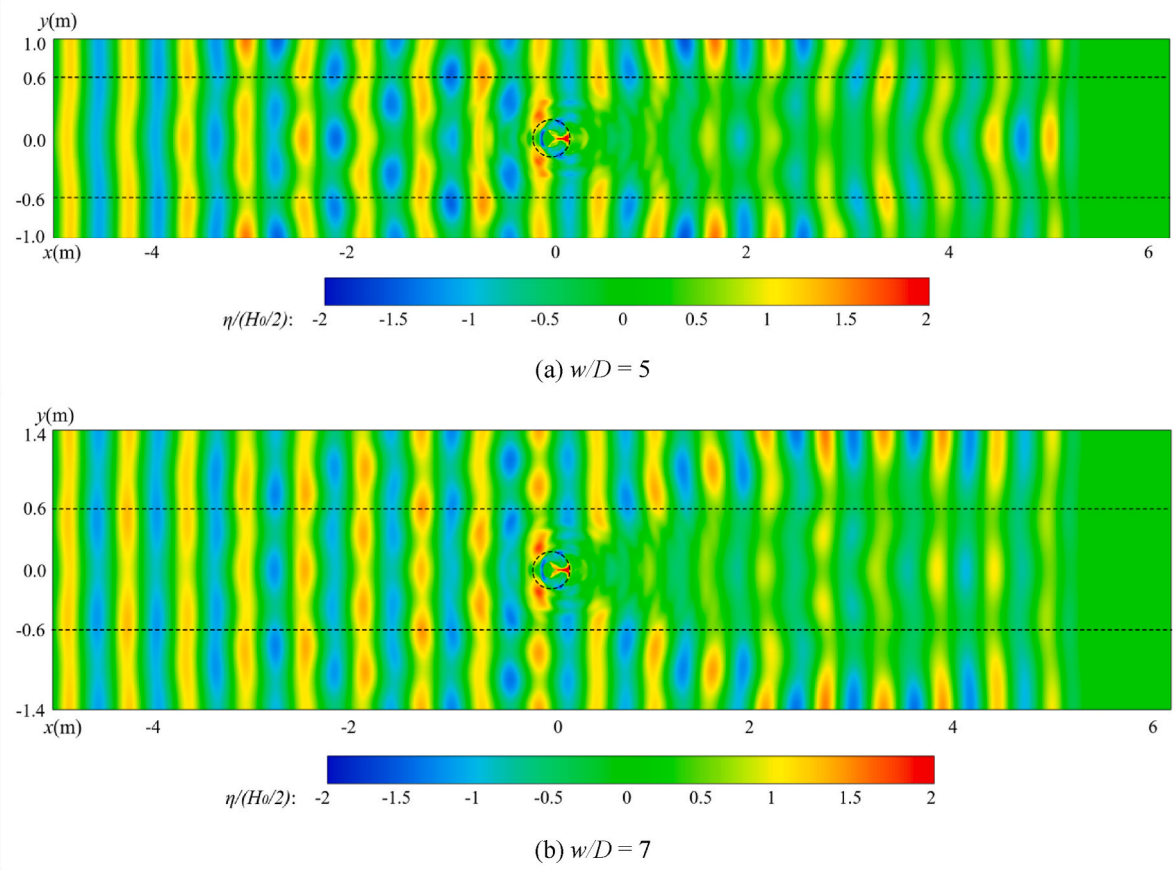

Fig. 16. Free surface elevation distributions for $w/D = 5$ and 7 at $t/T = 28.00$.

reflection becomes apparent around $x = 2$ m, whereas for $w/D = 7$, it appears much farther downstream, near $x = 4$ m. Following this reflection, the wave amplitude gradually recovers along the flume centreline, marking the end of the shadow zone. Therefore, while variations in flume width have a minimal effect on the wave focusing performance, they significantly influence the extent of the downstream wave shadow zone.

4.5. Effect of wave nonlinearity

The wave dynamics around the structure under the nonlinear wave condition are investigated through a series of simulations. The water depth is fixed at $h = 0.16$ m, while the incident wave height H_0 is systematically varied. A set of second-order Stokes waves with wave heights of 0.014 m, 0.016 m, 0.018 m, 0.020 m, 0.022 m, and 0.024 m are fed to the computational domain, all with a wavelength of $L_0 = 0.6$ m and frequency of $f = 1.55$ Hz.

Fig. 17 depicts the free surface elevations at the three gauges for different incident wave heights. As H_0 increases, gauge 1 records incident wave profiles that exhibit second-order nonlinear features, showing modest but progressively stronger crest sharpening and trough flattening features. This trend is consistent with the second-order Stokes theory, with the disparity between the crest and trough heights increased from 17 % to 30 %. Over the structure, the waveforms become more asymmetric, with the disparities between the crest and trough heights typically ranging from 50 % to 60 %, accompanied by wave height amplification. At gauge 4, the wave amplitude is consistently reduced, suggesting persistent wave sheltering across all nonlinear cases. In addition, the phase differences between the wave profiles at gauges 3 and 4 and those at gauge 1 increase with the incident wave height, indicating a faster propagation of the steeper waves around the structure.

Fig. 18 presents the averaged wave heights at the three gauges, with the linear wave case ($H_0 = 0.007$ m) included for reference. At gauge 1, the wave heights closely match the theoretical values, with deviations under 10 % in all cases. This confirms both the accuracy of the nonlinear wave generation algorithm and the adequacy of the domain size in preventing inlet reflection. Significant wave amplification is observed at gauge 3 in most cases, typically reaching over 1.5 times the incident wave height. However, this effect becomes less pronounced with increasing H_0, underscoring the importance of considering nonlinear effects in practical structural designs. In the wave shadow zone, the wave heights consistently remain below 50 % of the incident heights. Notably, when $H_0 = 0.024$ m, energy concentration within the structure becomes minimal, yet the wave sheltering effect persists downstream. This may suggest the presence of additional energy dissipation mechanisms, such as wave breaking or other forms of nonlinear energy loss. A higher incident wave height may lead to significant wave breaking and turbulence, which are beyond the scope of the current laminar flow model. Future studies will incorporate turbulence models to explore the transition from non-breaking to breaking waves and to more accurately resolve the nonlinear processes associated with wave breaking.

Fig. 19 illustrates the free surface elevation distributions at different instants within a wave cycle for the case of $H_0 = 0.024$ m. In contrast to the short-crested wave patterns observed in the linear case, the wavefronts here remain largely straight and continuous throughout the domain. The effect of wave refraction is significantly diminished, allowing the waves to pass smoothly along the sides of the structure with minimal distortion. This is consistent with the comparable wave height to the incident wave at gauge 3 in Fig. 18. Downstream of the structure, the wave rapidly reverts back to its incident wave pattern, resulting in a noticeably smaller wave shadow zone.

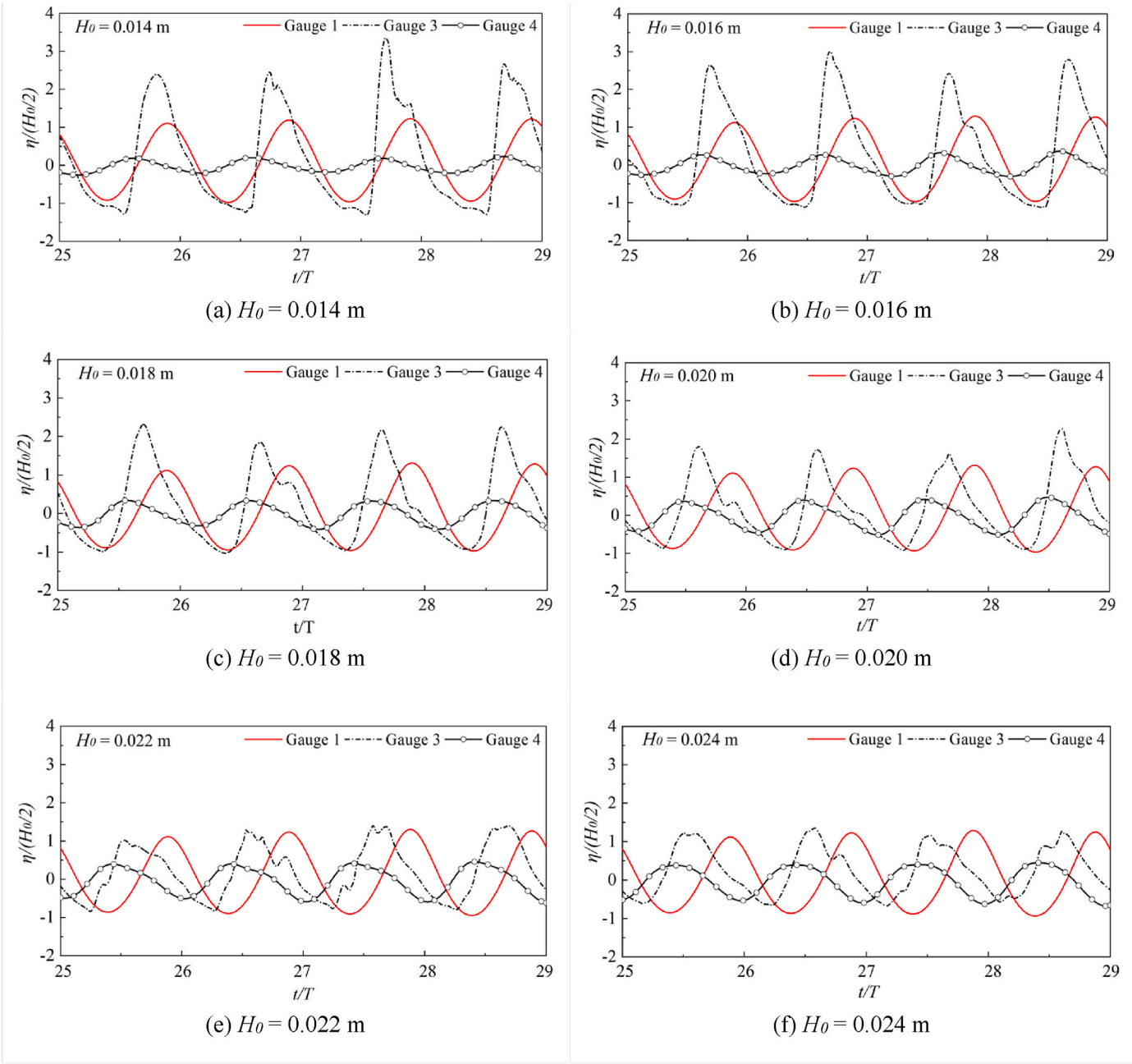

Fig. 17. Free surface elevations at various incident wave heights.

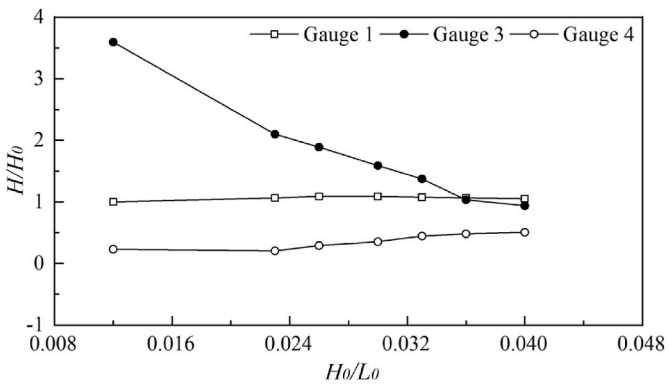

Fig. 18. Averaged wave heights at the three gauges.

To quantify the streamwise shortening of the shadow zone, an additional gauge (gauge 5) is placed further downstream at $x = 1.25$ m along the flume centreline. Fig. 20 compares the free surface elevations at this gauge for $H_0 = 0.007$, 0.016, 0.020, and 0.024 m. In the linear wave case, the wave amplitude reduces to approximately 60 % of the incident amplitude, whereas under the nonlinear wave condition, it reaches or even slightly exceeds the incident level. This increase may result from the nonlinear interaction between the refracted and reflected waves. In addition, a significant phase shift is seen, suggesting that the downstream wave propagation becomes faster as the incident wave height increases. These results demonstrate that the wave profile recovers more quickly to the incident form under the nonlinear wave condition, and the shadow zone ends at a shorter distance from the structure, i.e., 3.2 times the cylinder diameter. Hence, increasing wave nonlinearity has an adverse effect on the extent of the shadow zone.

Fig. 21 presents the velocity fields around the structure for $H_0 =$

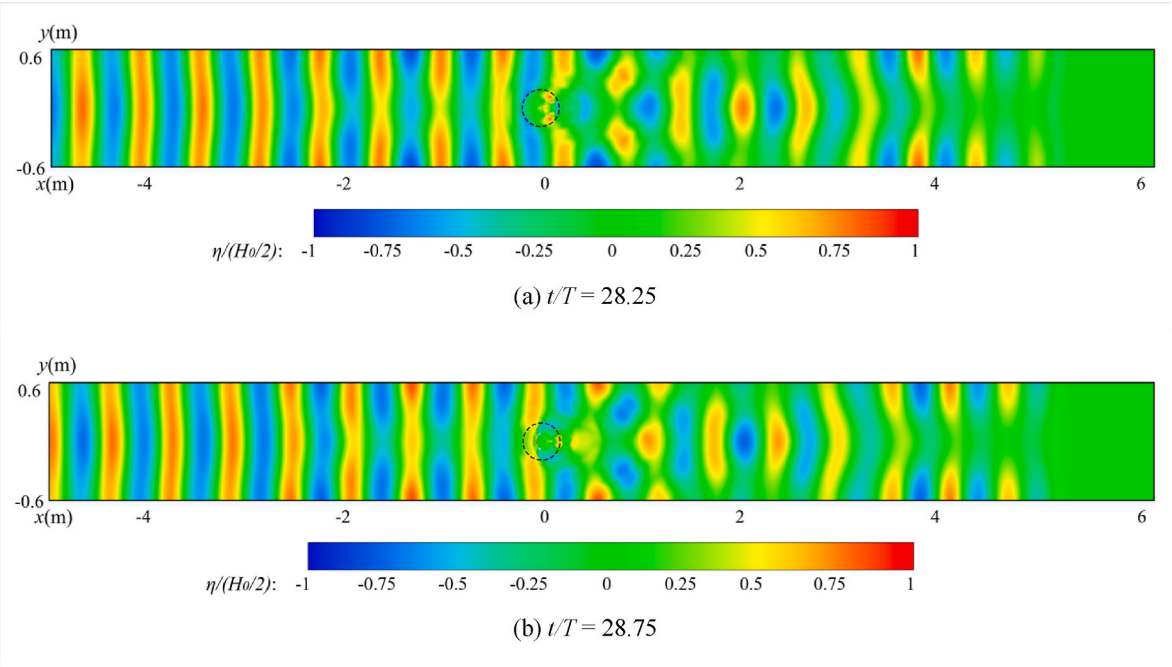

Fig. 19. Free surface elevation distributions for $H_0 = 0.024$ m.

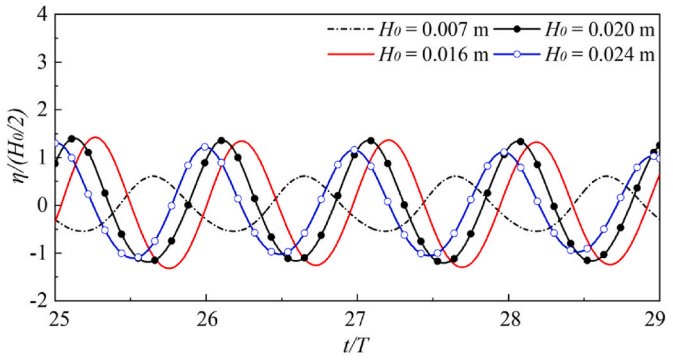

Fig. 20. Free surface elevations at gauge 5 for various incident wave heights.

0.024 m at two representative instants. Compared with the linear wave case, the weakened refraction effect allows fluid particles on both sides of the structure to oscillate largely undisturbed, while the destructive interference among the refracted wave components occurs only within a limited region immediately behind the cylinder. In addition, although local flow acceleration can still be observed within the shadow zone, the increase in fluid velocity is less pronounced, and the fluid motion rapidly returns to the incident wave pattern. These features explain the minimal wave amplification over the structure and the shortened extent of the shadow zone downstream.

5. Conclusions

A CFD model has been developed to systematically investigate the performance of a metamaterial-inspired structure. The multi-layered cylindrical structure alters the local water depth and thus the wave propagation, enabling wave energy concentration within a small area while generating a downstream shadow zone with significantly reduced wave amplitude. The numerical model is validated against the experimental measurements across a range of water depths.

A comparative analysis between the multi-layered and single-layered configurations highlights the effectiveness of the designed water depth profile in redistributing wave energy. In the multi-layered configuration, wave amplification is more pronounced, with the wave height reaching up to 3.6 times the incident value over the structure due to refraction, while the wave height in the shadow zone decreases by approximately 80 %. This sheltering is attributed to the destructive interference among the refracted wave components, which facilitates the conversion from potential energy to kinetic energy. In contrast, with the single-layered configuration, the downstream wave amplitude increases to 1.8 times the incident amplitude, with no shadow zone observed.

Parametric studies have been performed to examine the impact of key factors, such as the water depth, wave frequency, flume width and wave height, on the wave focusing and sheltering effects of the structure. Changing the depths reduces the wave amplification over the cylinder and promotes the recovery of the downstream wave to the incident profile. At a depth of 0.15 m, diffraction becomes dominant around the cylinder, reducing the shadow zone length by a half of that with the designed water depth. The higher-frequency waves observe more significant amplification and stronger downstream attenuation. Nevertheless, across all frequency cases, the wave amplitude typically reaches 2–3 times the incident amplitude, confirming the structure's robust performance over a moderate frequency range. A wider flume delays the reflection at the sidewalls, resulting in a notable extension of the shadow zone. Under the second-order Stokes wave condition, the asymmetry of the incident waveform is significantly amplified over the structure, with the disparity between the crest and trough heights reaching 50 %–60 %. Yet, this effect becomes less prominent with an increase in the incident wave height. Compared to the linear case, the downstream wave profile also reverts more quickly to the incident wave form, and the shadow zone ends at a shorter distance from the structure, i.e., 3.2 times the cylinder diameter.

This study demonstrates the potential of the multi-layered cylindrical structure in developing efficient, integrated breakwater-WEC systems. The wave shadow zone produced by the compact structure offers effective protection to coastal infrastructure. Simultaneously, placing WECs at the focal point of the structure enhances energy harvesting efficiency, further reducing wave forces and run-up and allowing for shared construction and maintenance costs. This approach offers a cost-effective solution for the combined goals of wave energy utilisation and coastal protection. In future research, we will integrate a cylindrical

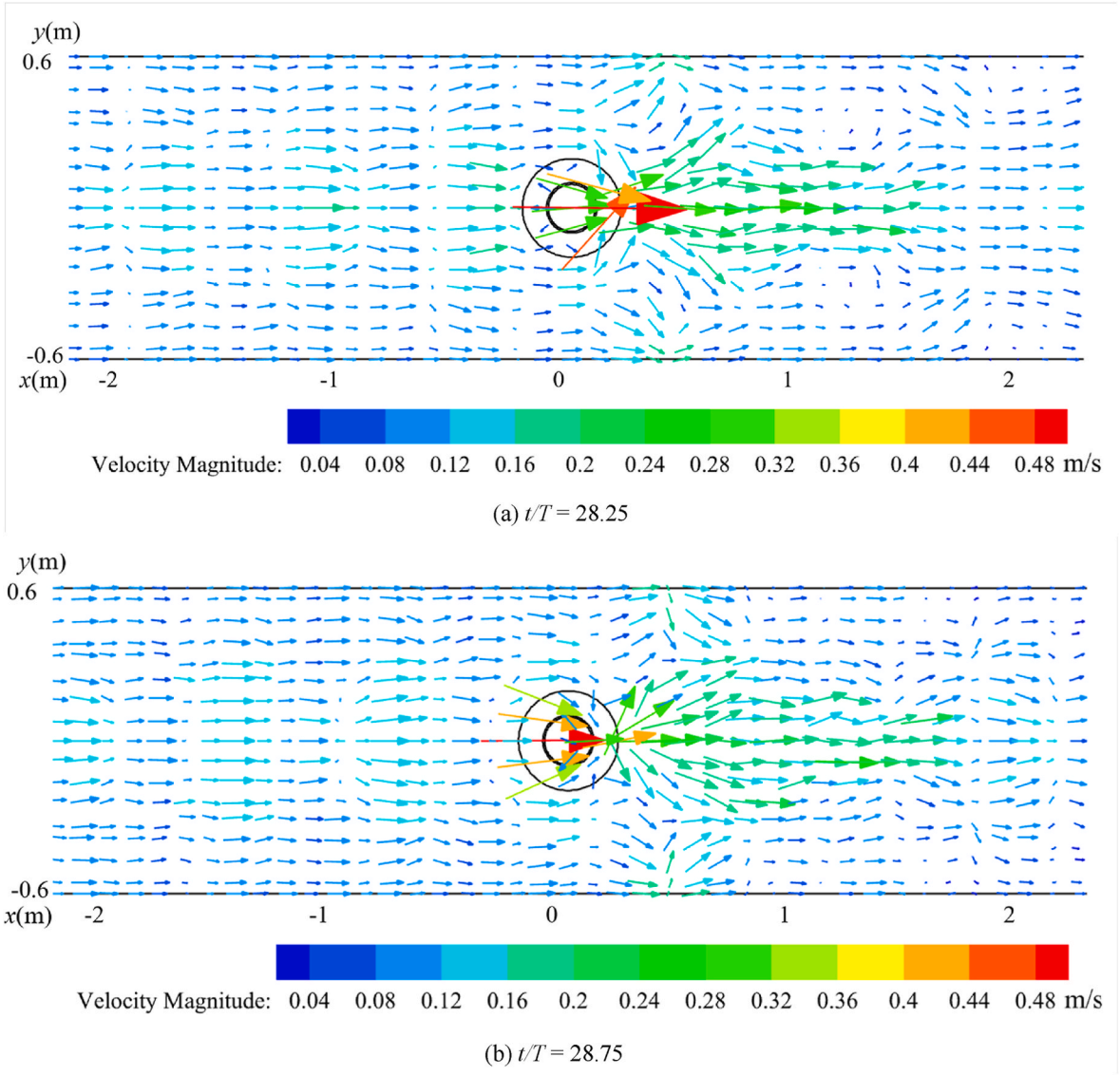

Fig. 21. Velocity fields at the still water level around the structure for $H_0 = 0.024$ m.

OWC (oscillating water column) model into our simulations and examine the joint performance of the OWC and structure. Moreover, while the present study assumes a flat seabed to focus on the structural effects, future investigations will examine the influence of seabed slopes and irregular bathymetries, which may alter the refraction pattern and shift the focal locations. These studies, together with irregular wave scenarios based on widely-used spectra (e.g., JONSWAP, Pierson–Moskowitz), will further assess the structure's applicability in realistic marine environments.

CRediT authorship contribution statement

Yuhao Cen: Writing – original draft, Software, Methodology, Investigation, Conceptualization. **Dongfang Liang:** Writing – review & editing, Supervision, Funding acquisition. **Yifeng Yang:** Writing – review & editing, Validation, Investigation. **Xiaodong Liu:** Writing – review & editing, Software, Methodology.

Declaration of competing interest

The authors declare that they have no known competing financial interests or personal relationships that could have appeared to influence the work reported in this paper.

Acknowledgments

We are grateful for the financial support from the Royal Society International Exchange Project (IEC\NSFC\242411) and the National Natural Science Foundation of China (W2421072). For the purpose of open access, the authors have applied a Creative Commons Attribution (CC BY) license to any Author Accepted Manuscript version arising from this submission.

Data availability

All data underlying the results are available as part of the article and no additional source data are required.

References

Berraquero, C.P., Maurel, A., Petitjeans, P., Pagneux, V., 2013. Experimental realization of a water-wave metamaterial shifter. Phys. Rev. E 88, 051002. https://doi.org/10.1103/PhysRevE.88.051002.

Calheiros-Cabral, T., Rosa-Santos, P., Taveira-Pinto, F., Lara, J.L., 2025. Harnessing wave energy through breakwater integration: a review of technologies, deployment

strategies and an open-access database. Renew. Sustain. Energy Rev. 223, 115975. https://doi.org/10.1016/j.rser.2025.115975.
Cen, Y., Liang, D., Cheng, Q., Liu, X., Zou, S., 2024a. Hydrodynamic performance of shallow-water waveguides subject to nonlinear waves. Phys. Fluids 36, 047108. https://doi.org/10.1063/5.0198853.
Cen, Y., Ma, J., Liu, X., Liang, D., 2024b. Parametric study of the performance of an annular water wave concentrator. Phys. Fluids 36, 097144. https://doi.org/10.1063/5.0226745.
Chen, H., Chan, C.T., 2007. Transformation media that rotate electromagnetic fields. Appl. Phys. Lett. 90, 241105. https://doi.org/10.1063/1.2748302.
Chen, H., Yang, J., Zi, J., Chan, C.T., 2009. Transformation media for linear liquid surface waves. EPL 85, 24004. https://doi.org/10.1209/0295-5075/85/24004.
Constantin, P., Foiaş, C., 1988. Navier-Stokes Equations. University of Chicago Press.
Cummer, S.A., Christensen, J., Alù, A., 2016. Controlling sound with acoustic metamaterials. Nat. Rev. Mater. 1, 16001. https://doi.org/10.1038/natrevmats.2016.1.
De Vita, F., De Lillo, F., Bosia, F., Onorato, M., 2021. Attenuating surface gravity waves with mechanical metamaterials. Phys. Fluids 33, 047113. https://doi.org/10.1063/5.0048613.
Dupont, G., Guenneau, S., Kimmoun, O., Molin, B., Enoch, S., 2016. Cloaking a vertical cylinder via homogenization in the mild-slope equation. J. Fluid Mech. 796. https://doi.org/10.1017/jfm.2016.249.
Dupont, G., Kimmoun, O., Molin, B., Guenneau, S., Enoch, S., 2015. Numerical and experimental study of an invisibility carpet in a water channel. Phys. Rev. E 91, 023010. https://doi.org/10.1103/PhysRevE.91.023010.
Fluent, A., 2011. Ansys Fluent Theory Guide. ANSYS Inc.
Green, M.A., Pillai, S., 2012. Harnessing plasmonics for solar cells. Nat. Photonics 6, 130–132. https://doi.org/10.1038/nphoton.2012.30.
Hao, J., Li, J., Liu, S., Wang, L., 2022. Wave amplification caused by Bragg resonance on parabolic-type topography. Ocean Eng. 244. https://doi.org/10.1016/j.oceaneng.2021.110442.
Holthuijsen, L.H., 2010. Waves in Oceanic and Coastal Waters. Cambridge University Press.
Kinkhabwala, A., Yu, Z., Fan, S., Avlasevich, Y., Müllen, K., Moerner, W.E., 2009. Large single-molecule fluorescence enhancements produced by a bowtie nanoantenna. Nat. Photonics 3, 654–657. https://doi.org/10.1038/nphoton.2009.187.
Lai, Y., Ng, J., Chen, H., Han, D., Xiao, J., Zhang, Z.Q., Chan, C.T., 2009. Illusion optics: the optical transformation of an object into another object. Phys. Rev. Lett. 102, 1–4. https://doi.org/10.1103/PhysRevLett.102.253902.
Lee, S.H., Park, C.M., Seo, Y.M., Kim, C.K., 2010. Reversed doppler effect in double negative metamaterials. Phys. Rev. B 81, 1–4. https://doi.org/10.1103/PhysRevB.81.241102.
Li, C., Xu, L., Zhu, L., Zou, S., Liu, Q.H., Wang, Z., Chen, H., 2018. Concentrators for water waves. Phys. Rev. Lett. 121, 104501. https://doi.org/10.1103/PhysRevLett.121.104501.
Liberal, I., Engheta, N., 2017. Near-zero refractive index photonics. Nat. Photonics 11, 149–158. https://doi.org/10.1038/nphoton.2017.13.
Lighthill, J., 1988. Fundamentals concerning wave loading on offshore structures. J. Fluid Mech. 173, 667–681. https://doi.org/10.1016/b978-0-08-036232-8.50007-4.
Loo, C., Lowery, A., Halas, N., West, J., Drezek, R., 2005. Immunotargeted nanoshells for integrated cancer imaging and therapy. Nano Lett. 5, 709–711. https://doi.org/10.1021/nl050127s.
Ma, G., Sheng, P., 2016. Acoustic metamaterials: from local resonances to broad Horizons. Sci. Adv. 2. https://doi.org/10.1126/sciadv.1501595.
Ma, H.F., Cui, T.J., 2010. Three-dimensional broadband ground-plane cloak made of metamaterials. Nat. Commun. 1. https://doi.org/10.1038/ncomms1023.
Martinelli, L., Ruol, P., Zanuttigh, B., 2008. Wave basin experiments on floating breakwaters with different layouts. Appl. Ocean Res. 30, 199–207. https://doi.org/10.1016/j.apor.2008.09.002.
Maurel, A., Marigo, J.J., Cobelli, P., Petitjeans, P., Pagneux, V., 2017. Revisiting the anisotropy of metamaterials for water waves. Phys. Rev. B 96, 1–8. https://doi.org/10.1103/PhysRevB.96.134310.
Mei, C., Stiassnie, M., Yue, D., 2005. Theory and applications of Ocean surface waves: part 1: Linear aspects. World Scientif. https://doi.org/10.4324/9781003046998-1.
Pendry, J.B., 2000. Negative refraction makes a perfect lens. Phys. Rev. Lett. 85, 3966. https://doi.org/10.1103/PhysRevLett.85.3966.
Qian, C., Lin, X., Yang, Y., Xiong, X., Wang, H., Li, E., Kaminer, I., Zhang, B., Chen, H., 2019. Experimental observation of superscattering. Phys. Rev. Lett. 122, 63901. https://doi.org/10.1103/PhysRevLett.122.063901.
Qin, Z., Qian, C., Shen, L., Wang, X., Kaminer, I., Chen, H., Wang, H., 2023. Superscattering of water waves. Natl. Sci. Rev. 10. https://doi.org/10.1093/nsr/nwac255.
Ren, J., Jin, P., Liu, Y., Zang, J., 2021. Wave attenuation and focusing by a parabolic arc pontoon breakwater. Energy 217, 119405. https://doi.org/10.1016/j.energy.2020.119405.
Schurig, D., Mock, J.J., Justice, B.J., Cummer, S.A., Pendry, J.B., Starr, A.F., Smith, D.R., 2006. Metamaterial electromagnetic cloak at microwave frequencies. Science 314, 977–980. https://doi.org/10.1126/science.1133628.
Scruggs, J., Jacob, P., 2009. Harvesting Ocean wave energy. Science 323, 1176–1178. https://doi.org/10.1126/science.1168245.
Sheng, P., Zhang, X.X., Liu, Z., Chan, C.T., 2003. Locally resonant sonic materials. Phys. B Condens. Matter 338, 201–205. https://doi.org/10.1016/S0921-4526(03)00487-3.
Shin, D., Urzhumov, Y., Jung, Y., Kang, G., Baek, S., Choi, M., Park, H., Kim, K., Smith, D. R., 2012. Broadband electromagnetic cloaking with smart metamaterials. Nat. Commun. 3, 1213. https://doi.org/10.1038/ncomms2219.
Smith, D.R., Pendry, J.B., Wiltshire, M.C.K., 2004. Metamaterials and negative refractive index. Science 305, 788–792. https://doi.org/10.1126/science.1096796.
Waldman, S., 2001. Detection of very small neutrino masses in double-beta decay using tagging. Int. J. Mod. Phys. A 16, 745–748. https://doi.org/10.1142/S0217751X01007972.
Wang, W., 1986. Electromagnetic Wave Theory. Google Scholar.
Xiao, S., Qiu, M., 2005. Doppler effects in a left-handed material: a first-principles theoretical study. Microw. Opt. Technol. Lett. 47, 76–79. https://doi.org/10.1002/mop.21086.
Yang, J., Tang, Y.F., Ouyang, C.F., Liu, X.H., Hu, X.H., Zi, J., 2009. Observation of the focusing of liquid surface waves. Appl. Phys. Lett. 95, 3–6. https://doi.org/10.1063/1.3222968.
Zareei, A., Alam, M.R., 2015. Cloaking in shallow-water waves via nonlinear medium transformation. J. Fluid Mech. 778, 273–287. https://doi.org/10.1017/jfm.2015.350.
Zhang, X., Liu, Z., 2008. Superlenses to overcome the diffraction limit. Nat. Mater. 7, 435–441. https://doi.org/10.1038/nmat2141.
Zhang, Z., He, G., Gou, Y., Luan, Z., Liu, S., He, R., 2023. Wavelength manipulation in shallow water via space transformation method. Phys. Fluids 35. https://doi.org/10.1063/5.0172013.
Zhang, Z., Liu, S., Luan, Z., Wang, Z., He, G., 2020. Invisibility concentrator for water waves. Phys. Fluids 32. https://doi.org/10.1063/5.0019129.
Zhao, X.L., Ning, D.Z., Zou, Q.P., Qiao, D.S., Cai, S.Q., 2019. Hybrid floating breakwater-WEC system: a review. Ocean Eng. 186, 106126. https://doi.org/10.1016/j.oceaneng.2019.106126.
Zhou, B., Zheng, Z., Jin, P., Wang, L., Zang, J., 2022. Wave attenuation and focusing performance of parallel twin parabolic arc floating breakwaters. Energy 260, 125164. https://doi.org/10.1016/j.energy.2022.125164.
Zhu, S., Zhao, X., Han, L., Zi, J., Hu, X., Chen, H., 2024. Controlling water waves with artificial structures. Nat. Rev. Phys. 6, 231–245. https://doi.org/10.1038/s42254-024-00701-8.
Zou, S., Xu, Y., Zatianina, R., Li, C., Liang, X., Zhu, L., Zhang, Y., Liu, G., Liu, Q.H., Chen, H., Wang, Z., 2019. Broadband waveguide cloak for water waves. Phys. Rev. Lett. 123, 74501. https://doi.org/10.1103/PhysRevLett.123.074501.